Title

Effective mechanical potential of cell–cell interaction explains basic structures of three-dimensional morphogenesis

Short title

Effective potential of cell–cell interaction during morphogenesis

Authors

Hiroshi Koyama[1,2,*], Hisashi Okumura[2,3,4], Atsushi M. Ito[5], Tetsuhisa Otani[2,6], Kazuyuki Nakamura[7,8], Kagayaki Kato[2,9,10], and Toshihiko Fujimori[1,2]

[1]Division of Embryology, National Institute for Basic Biology, 5-1 Higashiyama, Myodaiji, Okazaki, Aichi 444-8787, Japan

[2]SOKENDAI (The Graduate University for Advanced Studies), Hayama, Kanagawa 240-0193, Japan

[3]Biomolecular Dynamics Simulation Group, Exploratory Research Center on Life and Living Systems (ExCELLS), National Institutes of Natural Sciences, 5-1 Higashiyama, Myodaiji, Okazaki, Aichi 444-8787, Japan

[4]Institute for Molecular Science, National Institutes of Natural Sciences, 5-1 Higashiyama, Myodaiji, Okazaki, Aichi 444-8787, Japan

[5]Department of Helical Plasma Research, National Institute for Fusion Science, National Institutes of Natural Sciences, 322-6 Oroshi-cho, Toki, Gifu 509-5292, Japan

[6]Division of Cell Structure, National Institute for Physiological Sciences, 5-1 Higashiyama, Myodaiji, Okazaki, Aichi 444-8787, Japan

[7]School of Interdisciplinary Mathematical Sciences, Meiji University, 4-21-1 Nakano, Nakano-ku, Tokyo 164-8525, Japan

[8]JST, PRESTO, 4-1-8 Honcho, Kawaguchi, Saitama 332-0012, Japan

[9]Bioimage Informatics Group, Exploratory Research Center on Life and Living Systems (ExCELLS), National Institutes of Natural Sciences, 38 Nishigonaka, Myodaiji, Okazaki, Aichi 444-8585, Japan

[10]Laboratory of biological diversity, National Institute for Basic Biology, 38 Nishigonaka, Myodaiji, Okazaki, Aichi 444-8585, Japan

*Correspondence: Hiroshi Koyama

Division of Embryology, National Institute for Basic Biology, 5-1 Higashiyama, Myodaiji, Okazaki, Aichi 444-8787, Japan

Phone: +81 564 59 5862,

hkoyama@nibb.ac.jp.

Author contribution

H.K. designed the work, H.K., A.M.I., and H.O. contributed to the conception. H.K. and T.F. designed experiments, T.O. provided experimental materials, and H.K. performed experiments and image processing. H.K. and H.O. designed models, H.K. developed computational algorithms, and H.K. and K.N. statistically analyzed the data. H.K., T.O., H.O., A.M.I., K.N., K.K., and T.F. wrote the manuscript, and all authors contributed to the interpretation of the results.

Conflicts of interest

The authors declare no competing financial interests.

Keywords

effective potential of cell–cell interaction, morphological diversity, mechanics, emergent property of multi-cellular system, mouse pre-implantation embryo

This PDF file includes:

Main text

Figure 1 to 10

-

Supplementary information (text and supplementary Figures and Table)

Abstract

Mechanical forces of cell–cell interactions have been suggested to be critical for the emergence of diverse three-dimensional morphologies of multicellular organisms. The direct evaluation of the forces in living systems has been difficult due to technical limitations. Here, we developed a framework for inferring and modeling mechanical forces of cell–cell interactions. First, by analogy to coarse-grained models in molecular and colloidal sciences, cells were assumed to be spherical particles, where the mean forces (i.e. effective forces) of pairwise cell–cell interactions were considered. Then, the forces were statistically inferred from live imaging data, and subsequently, we successfully detected effective mechanical potentials of cell–cell interactions as a function of the cell–cell distances in Madin-Darby canine kidney (MDCK) cells, *C.elegans* early embryos, and mouse pre-implantation embryos. The qualitative and quantitative differences in the inferred potentials can be a control parameter for morphological transition during the mouse compaction process, and can also reproduce various three-dimensional morphologies including aggregates, cavities, tubes, cups, and two-dimensional sheets, which constitute basic structures observed during morphogenesis. We propose that effective potentials of cell–cell interactions are measurable, and their qualitative and quantitative features are critical for the emergence

84 of diverse three-dimensional morphogenesis.

85

Significance statement

Emergence of diverse morphologies of multicellular organisms is one of the most intriguing phenomena in nature. Mechanical forces generated by cells play central roles in morphogenesis, however, their measurement is technically limited. Furthermore, due to the complex situations in living systems, a model for describing the emergent properties of multicellular systems has not been established. Here, we developed a method for inferring mechanical potential energy of cell–cell interactions, and showed that the quantitative differences in the potential is alone sufficient to describe basic three-dimensional morphologies observed during embryogenesis and organogenesis. This framework sheds light on the emergent properties of multicellular systems.

Introduction

In multi-cellular living systems, various three-dimensional morphologies are observed. The emergence of these diverse morphologies is thought to be primarily dependent on the mechanical properties of the constituent cells. In particular, mechanical forces of cell–cell interactions are involved in morphogenetic events such as epithelial cell movement and cell sorting (1–5). However, the mechanical basis of morphogenesis, which gives rise to a variety of structures, remains to be elucidated.

The mechanical forces of cell–cell interactions are regulated by various factors. In epithelial cells, whose shapes are typically columnar polygons, cell–cell adhesion energy is controlled by cadherin family proteins (1, 2, 6). Moreover, cellular polarities such as apico-basal polarity are linked to biased localization of cadherin proteins, leading to directional differences in the forces of cell–cell interactions. In addition to these direct interactions, there are indirect interactions through external factors. In mesenchymal cells, cell–cell interactions are regulated through extracellular matrix (i.e. substrate) originally generated by the cells (7–9). Therefore, cell–cell interactions entail many microscopic parameters determined by various proteins and cellular processes, resulting in very complex physics with many degrees of freedom. To elucidate the principles underlying the emergence of morphological diversity, it is essential to

117 investigate how these cellular features can be described by models with simple meso or
118 macroscopic parameters.

119 The mechanical potential of cell–cell interaction is conceptually well
120 recognized, and has been used in theoretical studies where various potentials such as a
121 hard- or soft-core potential were considered (Fig. 1A-B) (7, 10–18). Although adhesive
122 forces between two isolated cells have been measured (i.e. forces required to dissociate
123 one cell from the other) (4, 19), they have neither been measured nor inferred in more
124 complex multi-cellular systems, which differ from isolated cells as the consequences of
125 the cell polarities, the indirect interactions, etc. If effective potentials of cell–cell
126 interactions could be defined as a model integrating these various factors (Fig. 1C), the
127 effective potentials would be useful to explain the emergence of morphological diversity
128 of multi-cellular systems. However, it is challenging to identify all these factors and
129 measure the values of their related-parameters, which is a bottleneck to obtain effective
130 potentials through bottom-up approaches. Consequently, it remains poorly understood
131 whether qualitative and quantitative differences in the effective potentials are detectable
132 in living systems and whether the differences can explain the emergence of various
133 three-dimensional morphologies.

134 In this study, by analogy to non-living materials (Fig. 1D-G), we tried a

top-down approach: we developed a method for statistically inferring the effective potential of cell–cell interactions using nuclear tracking data from live imaging as reference data, which are relatively easy to obtain. Thus, shapes and polarities of cells were not explicitly considered at this moment, whose effects we tried to decode after acquiring inference results (Fig. 1I). Our method was validated by using various simulation data with or without external factors including egg shells and cavities. Influence of boundary conditions such as egg shells on the inference results was revealed to be negligible. Then, we tested whether effective potentials of cell–cell interactions can be detected in living systems. We applied this method to relatively small multi-cellular systems (4–350 cells) including mouse pre-implantation embryos and early embryos of the nematode *Caenorhabditis elegans*. We clearly detected effective potentials as a function of cell–cell distances in these systems. Importantly, we identified a control parameter from the effective potentials, which can describe morphological transition during the compaction of the mouse embryos. Further theoretical analyses demonstrated that effective potential can reproduce various structures including cell aggregates, cavities, tubes, cups (round and hollow shapes), and two-dimensional sheets (Fig. 1H). The inferred potentials would be useful to predict cellular behaviors and mechanical properties of the systems.

153

Theory and principle for inferring effective potential

Overview of strategy for inferring effective potentials/forces of cell–cell interaction

To measure or infer the effective potentials or forces of cell–cell interactions *in vivo*, we developed a particle-based cell model in which attractive or repulsive forces are exerted between each pair of cells (Fig. 1A, B and D). This coarse-grained model does not explicitly incorporate microscopic features of cells such as cell shape, polarities, size, heterogeneity, cell type or origin (e.g., epithelial, mesenchymal, or blastomere cells), etc. (Fig. 1C). Simultaneously, we obtained time series of three-dimensional cell positions from confocal microscopic images (Fig. 1E) and statistically inferred the forces of cell–cell interactions by systematically searching for force values that could reproduce the cell movements observed *in vivo* (Fig. 1F). To validate the method, we utilized synthetic data generated by simulations under given potentials of cell–cell interactions, and confirmed that the inferred forces were consistent with the given-potentials. The details of each part of the analysis are explained in the following sections.

Particle-based cell models

In our model, particles interact with each other and attractive or repulsive

172 forces (F_i) are assumed (Fig. 1D), where i is an identifier for particle–particle
173 interactions. In three-dimensional cellular systems with no attachment to substrates, we
174 did not assume persistent random walks which are originated from cellular traction
175 forces on substrates (20, 21).

176 The equation of particle motions is defined below. In cellular-level phenomena,
177 viscous drag force or frictional force provided by the surrounding medium or tissue is
178 dominant, as expected from the low Reynolds number; consequently, the inertial force is
179 negligible in general (3, 7, 9, 22, 23). The forces in such a system can be assumed to be
180 correlated with the velocities of the objects (3, 9, 15, 24, 25). Thus, the velocity (V_p) of
181 a particle is calculated by the net force (F_p) exerted on the particle as follows:

182 $$V_p = F_p / \gamma \qquad \text{(Eq. 1)},$$

183 where p is an identifier for particles and γ is the coefficient of viscous drag and
184 frictional forces. F_p is the summation of F_i: $F_p = \sum_{i=1}^{I} \delta(p) F_i$, where I is the total number
185 of interactions, and in the case that the ith interaction is formed with the pth particle,
186 $\delta(p)$ is 1, otherwise $\delta(p)$ is 0 (Fig. 1D). We assumed the simplest situation, i.e., γ is
187 constant (=1.0). Thus, by giving the values of F_i from, for instance, a distance–potential
188 curve, a simulation can run.

189

190 *Data acquisition of time series of cell positions*

191 To define cell positions, we focused on nuclei, because they are most easily
192 imaged by microscopy (Fig. 1E) in a wide range of organisms from *C. elegans* to
193 mammals, and these data are accumulating (26–30). We utilized publicly available
194 nuclear tracking data of a developing embryo of *C. elegans* (26); nuclear tracking data
195 of developing mouse embryos and MDCK cultured cells were obtained in this study (SI,
196 Section 2, 8, and 11 with text data).

197

198 *Development of method for inferring effective potentials/forces of cell-cell interaction*

199 In the case of ions, molecules, etc., radial distribution functions are often
200 measured and used to infer the effective potentials of their interactions (31, 32).
201 Although this method is simple and applicable to thermodynamically equilibrium
202 systems, it is not suitable for non-equilibrium systems, including morphogenetic events.
203 To infer the effective potentials of non-equilibrium systems, we fitted the particle-based
204 cell model to the time series of nuclear positions in the spirit of data assimilation, where
205 the fitting parameters are forces between all pairs of cell–cell interactions (the total
206 number is I, as previously defined) for each time frame. Data assimilation is a technique
207 to solve an inverse problem for a simulation-based model (33, 34). One of well-known

208 model fittings is based on least squares in combination with a linear model

209 (function-based model), resulting in inference of parameter values of the linear function.

210 In data assimilation, models to be fitted are simulation-based models instead of

211 function-based models, whereas least squares are also often used to infer parameter

212 values which are usually numerically solved. Through repeated cycles of simulations of

213 the model, we systematically searched for the values of the effective forces between all

214 pairs of cell–cell interactions that minimized the differences (i.e. corresponding to least

215 squares) between the particle positions in the simulations and the *in vivo* nuclear

216 positions (Fig. 1). The differences (G_{xyz}) to be minimized are defined as follows (SI,

217 Section 4-1 and 4-2).

218 $$G_{xyz} = \sum_{t=1}^{T} \sum_{p=1}^{P(t)} \frac{\left\{x_p(t) - x_p^{\mathrm{ref}}(t)\right\}^2 + \left\{y_p(t) - y_p^{\mathrm{ref}}(t)\right\}^2 + \left\{z_p(t) - z_p^{\mathrm{ref}}(t)\right\}^2}{\Delta t}$$

219 (Eq. 2)

220 Here, p is an identifier for particles, t is an identifier for time frames, and Δt is

221 the time interval between the time frames. The x, y, and z coordinates of the pth particle

222 obtained from microscopic images are x_p^{ref}, y_p^{ref}, and z_p^{ref}; ref means reference (Fig.

223 S2C). The coordinates during the repeated cycles of simulations are x_p, y_p, and z_p. The

224 effective forces were inferred for each cell–cell pair for each time frame (Fig. S2B and

225 C). Note that, because γ was assumed to be constant in Equation 1, we can only infer

relative but not absolute values of effective forces.

To determine whether our method can correctly infer effective forces, we first applied it to synthetic data generated by simulations under given potentials of particle–particle interactions, and examined whether the inferred effective forces were consistent with the given potentials (Fig. S3A). We tried the Lenard–Jones (LJ) potential as a test case of the given potentials. We applied the inference method to the time series of the simulation data, yielding effective forces for each pair of particles for each time frame (Fig. S3B). The inferred effective forces were plotted against particle–particle distance (Fig. S2D, S3C, and SI, Section 5). By averaging the plots for each shallow bin of distances, we obtained distance–force (DF) curves (Fig. S3C). We found that the DF curves were not consistent with the curve from the LJ potentials, suggesting that Equation 2 was not optimal. Therefore, we tried to incorporate various additional constraints (i.e. cost functions during the minimization procedures) into Equation 2. We found that, when a cost function was set so that force values approach zero at long distant regions of cell–cell interactions (Equation 3 and SI, Section 4-3), inferred DF curves became consistent with that from the LJ potentials (Fig. S3). The cost function is as follows:

$$G = G_{xyz} + G_{F_0} \qquad (G_{F_0} = \omega_{F_0} \sum_{t=1}^{T} \sum_{i=1}^{I(t)} \psi(D_i) F_i^2 \Delta t) \qquad \text{(Eq. 3)},$$

where the cell–cell interaction ID (i) defined in each time frame is from 1 to $I(t)$, D_i is the cell–cell distance of the ith interaction, and ω_{F_0} is a coefficient for determining the relative contribution of the second term to G. $\Psi(D_i)$ is a distance-dependent weight that increases gradually toward the cut-off distance and eventually becomes extremely large, defined as Equation S4 and Figure S2A-iii. Detailed principles, rational, and procedures are described in SI (Section 4). Additionally, if this cost function was not incorporated, this minimization problem exhibited indefiniteness (i.e., a unique solution could not be determined) and over-fitting also occurred. This cost function is considered as the prior in the Bayesian inference, and, in general, a unique solution could be ensured by introducing such a prior (33).

Using Equation S6 containing the above cost function (SI, Section 4-3), we also tried other potentials generated by freehand drawing, called "FH" potentials in this study, as an alternative to the LJ potentials (Fig. S3A and Movie S1B). The FH potentials were chosen because the simulation outcomes under the FH potentials differ from those under the LJ potentials as shown later (Fig. S12). The inferred DF curves were almost consistent with the given potentials (Fig. S3C, E, and SI, Section 4-3-4). Conversely, we also used time series of random–walk simulations as negative controls (Fig. S3A and Movie S1C), resulting in DF curves with zigzag and disorganized profiles

(Fig. S3C and E). Similar disorganized profiles were also detected in two-dimensional cellular systems where each cell almost randomly migrates due to its self-propelled activity under negligible cell–cell interactions (Fig. S5). These results indicate that our method can correctly infer DF curves.

Results

Systematic validation of inference method using simulation data

We first systematically validated our inference method using simulation data which include various external factors. Specifically, we assessed whether spatial constraints such as egg shells or cavities can affect inference results of effective forces of cell–cell interactions. Similar to the previous section, we generated simulation data under LJ potential, to which we applied our inference method.

In the absence of spatial constraints, inferred distance–force (DF) curves were well consistent with the DF curves derived from the LJ potential under various settings of simulations: the settings are related to time interval of sampling, cell proliferation, and fluctuation of forces between cell–cell interactions (Fig. 2A-B, S4, SI, Section 4-4, 7-4, and Movie S8A-B). Next, we introduced spatial constraints corresponding to egg

shells (SI, section 7-4-2 and Movie S8C). Even under narrow cylindrical constraints, inferred DF curves were well consistent with the DF curves from the LJ potential (Fig. 2C; length of cylinder = 25μm, S4, and SI, Section 4-4). By contrast, under constraints with smaller volume where each particle was highly compressed, the profiles of inferred DF curves were shifted leftward in the distance–force graph (Fig. 2C; length of cylinder = 15μm). This shift can be reasonable, if radial distribution functions under compressed conditions are considered. However, in cell biology, we think that the above compressive conditions are not physiologically relevant, because cells are essentially composed of non-compressive liquid and their volumes are not changed by external pressure. These results suggest that inferred DF curves are not significantly affected by boundary conditions provided from spatial constraints.

Next, we introduced cavities. Cells can generate cavities by secreting liquid, and then indirectly push other cells away (35–37), possibly resulting in indirect interactions. Although the generations of cavities are derived from the intrinsic features of cells under *in vivo* situations, we implemented cavities as spatial constraints under simulations. We assumed that particles located on the surface of a cavity cannot penetrate into the cavity (Fig. 2D, SI, S4, Section 7-4-2, and Movie S8D). Inferred DF curves were almost consistent with the DF curves from the LJ potential (Fig. 2D, S4,

298 and SI, Section 4-4). However, we detected additional repulsive forces at distant regions,
299 which we call distant energy barrier (DEB). Additionally, profiles similar to DEB are
300 well-known in molecular and colloidal sciences: by considering hydration of particles
301 by solvents as an external factor, effective potentials are modified so as to contain
302 energy barriers around distant regions (31, 32). We conclude that the cavities can
303 qualitatively change the profiles of effective potential of cell–cell interactions.

304 Related comprehensive analyses are provided in bioRxiv, doi:
305 https://doi.org/10.1101/812198, supporting that, despite the wide distributions of the
306 data points as shown by the heat maps, the inferred DF curves were reliable.

307

308 *Inference of effective forces in C. elegans early embryo*

309 We next investigated whether effective potential could be detected as a function
310 of cell–cell distance in three-dimensional *in vivo* systems. The nematode *C. elegans* has
311 well-defined embryogenesis: cell movements in early embryos are almost identical
312 among different individuals, and the time series of nuclear positions have been reported
313 previously (26). During early *C. elegans* embryogenesis, a fertilized egg (i.e. one cell)
314 repeatedly undergoes cell division and cell differentiation, ultimately forming an ovoid
315 embryo containing ~350 cells (Fig. S6A and Movie S3A). The cells become smaller

316 through cell division (38), and the total volume of the embryo remains constant because
317 the embryo is packed into a stiff egg shell. Thus, the volume of each cell is reduced by a
318 factor of 350 relative to the original egg, meaning that cell diameter is reduced by a
319 factor of 7. Because particle diameter is approximately reflected on a DF curve as the
320 distance with force = 0 (Fig. 1B) corresponding to the minimum of the potential, we
321 expected that inferred DF curves should be gradually shifted to the left side of the
322 distance–force graph throughout embryogenesis.

323 Figure 3A is a snapshot that shows nuclear positions and inferred effective
324 forces in the embryo; the temporal change is also visualized (Fig. S6B and Movie S3B),
325 where dynamic changes in the effective forces were observed. It was confirmed that our
326 inference problem has essentially a unique solution (Fig. 3B, S6D, and SI, Section 4-4).
327 We divided the whole embryogenesis into segments containing different time frames,
328 and obtained DF curves (Fig. 3C and S6C, time frame = 16–55, 36–75, 76–115, 116–
329 155, and 156–195). The DF curves exhibited organized patterns. All of the DF curves
330 had very similar profiles: repulsive and attractive forces were detected around the core
331 of the cells and longer interaction distances, respectively (Fig. 3D). We also calculated
332 the distance–potential (DP) curves by integrating the force values (Fig. 1B, S2D, and SI,
333 Section 5). Importantly, the distances at the minimum of the effective potentials were

334 gradually shifted toward the left side (Fig. 3D), as we had expected (Fig. 3E), indicating
335 that the inferred effective potentials were quantitatively consistent with the reduction in
336 cell volume during embryogenesis (Fig. 3E). Taken together, the patterns of the DP
337 curves seem to be physically reasonable.
338
339 *Effect of inferred distance–force curves on C.elegans embryonic morphologies*
340 We next investigated whether the simple DF curves can explain embryonic
341 morphologies. Because the dynamics of all cells during embryogenesis are very
342 complicated, largely due to the repeated cell division and cell differentiation, we
343 focused on a few typical features of the morphologies: aggregated cells and the ovoid
344 embryo shape. The embryonic cells can keep a cell aggregate even when the eggshell is
345 removed, and subsequent culture leads to a cell aggregate with an ovoid or distorted
346 shape, except for very early stage of development (< ~20 cells) (39, 40).
347 We performed simulations based on the particle-based cell model by
348 considering the DF curves, and investigated whether aggregated states with ovoid
349 shapes were stable. In multi-cellular systems, morphologies of systems are determined
350 by both DF curves and initial configurations, because energetic local minimum states
351 (i.e. metastable state) as well as global minimum states are meaningful. To find stable

352 states under the DF curves, we performed simulations starting from various initial
353 configurations of the particles, and the systems were relaxed. When we used the DF
354 curves obtained from the *C. elegans* embryos, we observed a tendency for the particles
355 to aggregate with an ovoid or distorted shape (Fig. 6A and S12). These results are
356 striking contrast to the simulation outcomes under the LJ or FH potential (Fig. S12).
357 These results suggest that the inferred effective DF curves are capable of recapitulating
358 the basic morphology of the *C. elegans* embryos.
359
360 *Inference of effective force in mouse pre-implantation embryos*
361 To further investigate whether effective forces could be obtained in
362 three-dimensional systems, we focused on mouse pre-implantation embryos, including
363 morulae at the 8-cell, compaction, and blastocyst stages (Fig. 4A, illustration). In 8-cell
364 stage embryos before compaction, cell–cell adhesion is weak, and individual cells can
365 be easily discerned (Fig. 4A, bright field). In the compaction-stage embryos composed
366 of ~16-32 cells, cell–cell adhesion becomes stronger due to elevated expression of
367 cadherin proteins on cell membrane, and the cells are strongly assembled (41). The
368 surface of the embryo becomes smooth, and the embryonic shape becomes more
369 spherical (Fig. 4A, bright field). In blastocyst-stage embryos composed of >64 cells, an

370 inner cavity is formed through liquid secretion from the cells, and the embryos expand
371 while maintaining their spherical shape. Trophectoderm (TE) cells form a single–
372 cell-layered structure at the outermost surface of the embryo, whereas the cells of the
373 inner cell mass (ICM) were tightly assembled, forming a cluster (Fig. 4A, illustration).

374 Figure 4B shows the snapshots of the inferred effective forces of cell–cell
375 interactions during the three embryonic stages that we examined (Movie S4D–G). The
376 uniqueness of the solutions was confirmed (Fig. S7B). We calculated the DF and DP
377 curves in a manner similar to *C. elegans* study described above, and obtained curves for
378 all three stages (Fig. 4C and D). The DF curves derived from the 8-cell and compaction
379 stages had typical profiles, with repulsive and attractive forces detected at short and
380 long interaction distances, respectively (Fig. 4D and S7A). On the other hand, the DF
381 curves derived from the blastocyst stage contained DEB (Fig. 4D, arrows), similar to
382 the case of simulation data considering a cavity (Fig. 2D). Moreover, when we inhibited
383 the cavitation by an inhibitor for Na^+/H^+ exchanger (S3226) (42), DEB was diminished
384 in the inferred potentials (Fig. S20), indicating that the cavity yielded the DEBs. These
385 results also indicate that the DF curves experience changes in their profiles during the
386 development.

387

388 *Effect of inferred distance–force curves on mouse embryonic morphologies*

389 We next asked whether the differences in the DF curves derived from the
390 mouse embryos were sufficient to explain the key morphological features of the
391 embryos. The DF curve derived from the compaction stage embryo yielded a spherical
392 shape where particles were aggregated (Fig. 6B and S12). In the case of the 8-cell stage
393 embryo, simulation results were similar to those obtained for the compaction stage,
394 except that the spherical shape seemed to be slightly distorted (Fig. S12). In the case of
395 the blastocyst stage embryo, when aggregated particles were given as initial
396 configurations, the particles gradually scattered and formed a spherical structure
397 harboring a cavity at the center (Fig. 6B). To examine whether DEB contribute to the
398 formation of a cavity, we artificially eliminated DEB from the inferred DF curves, and
399 performed a simulation. We found that no cavity was generated (Fig. 6B). These results
400 suggest that all of the DF curves from the various embryonic stages are sufficient to
401 explain their different morphologies. Nevertheless, because the DEB is not derived from
402 a "real" cell–cell interactions but from the indirect effect of the cavity (i.e. external
403 environment), we should notice that the predictive capabilities of the DP curves bearing
404 such DEBs would be limited.

405

Inference of effective distance–force curves and their effect on morphology in MDCK cyst

To further test the applicability of our method to structures harboring cavities, we focused on MDCK cells, derived from dog kidney epithelium, which can form cysts containing a cavity when cultured in suspension (Fig. 5A, illustration) or in gels composed of extracellular matrix (ECM) (43). To exclude adhesion between the cysts and the ECM, we chose suspension conditions in which a cyst can be assumed to be a mechanically isolated system. Figure 5D and S10 shows the DF and DP curves from a MDCK cyst. A DEB was detected in the DF curves, implying that a DEB is generally yielded in cavity-bearing structures.

Simulations based on inferred DF curves revealed that, a cavity was stably maintained in MDCK cells (Fig. 6C and S12). Moreover, the DF curves from which the DEB was artificially eliminated could not maintain the cavity-bearing structure (Fig. 6C). Taken together, the DF curves with the DEBs in the blastocyst and the MDCK cyst seem to reproduce the formation and maintenance of a cavity, respectively, though their predictive capabilities would be limited due to the indirect effect of the cavities.

Perturbation experiments for mouse compaction stage embryo

To evaluate the predictive capability of the DF curves inferred by our method, we performed perturbation experiments. In the mouse compaction stage, the cells are tightly assembled to form a spherical and symmetric embryonic shape. In other words, we think that there are two morphological features, 1) increase in symmetry of the embryos, and 2) smoothing of the embryonic surfaces. The embryos are surrounded by external structures called zona pellucida which are almost no effect on embryogenesis (44 and references therein). Because both E-cadherin and actomyosin are essential for the compaction process (41, 45, 46), we inhibited these proteins by chemicals: EDTA for E-cadherin, cytochalasin D for F-actin, and blebbistatin for non-muscle myosin II (Fig. 7A and S13).

The effective DP curves were inferred under these drugs (Fig. 7B and S13). Then, we quantitatively evaluated the differences among the DP curves and found that the distances at the potential minima were increased under the three inhibitors (Fig. 7C, left panel). This result predicted that the cell–cell distances were increased, that was supported through histological observations: each cell exhibited a nearly spherical shape and seemed that the cells were not so densely assembled especially under the condition of EDTA compared with the no-drugs condition (Fig. 7D and S16). The embryonic and cellular shapes are schematically depicted in Figure 7E. In addition, we found another

442 quantitative difference among the DP curves. We measured distances at 10% energy of
443 potential minima as relative values to the distances at the potential minima, and found
444 that the relative distances were decreased under EDTA and blebbistatin (Fig. 7C, right
445 panel, and S15A-B for other % energies). This result means that attractive forces of
446 long-range interactions were reduced under these drugs. Several other parameters were
447 also tested (Fig. S15).
448
449 *Predictive capability of effective potential for mouse compaction stage embryo*
450 Simulations under the DP curves from the drugs-treated embryos were
451 performed. The cell particles were spherically or almost spherically assembled under the
452 potentials of the normal embryos or the cytochalasin D-treated embryos, respectively
453 (Fig. 8A). By contrast, the cell particles were not spherically assembled under the
454 potentials of the EDTA or blebbistatin-treated embryos. All simulation data are provided
455 in Figure S17.
456 To relate the profiles of the DP curves to morphological changes in the
457 compaction process, we first introduced two indices for the morphologies as follows.
458 Sphericity ($=(36\pi V^2)^{1/3}/S$) is essentially defined as the ratio of volume (V) to surface
459 area (S) so that the value becomes 1.0 for spheres (SI, Section 7-1). Shapes other than

460 spheres show values less than 1.0. Thus, both the increases in symmetry and in
461 smoothness of surfaces contribute to this index. Aspect ratio is defined as the ratio of
462 the length of the longest axis to that of the shortest axis in an ellipsoid which is fitted to
463 an object of interest (SI, Section 7-1). The increase in symmetry leads to that the aspect
464 ratio becomes 1.0, and otherwise the aspect ratio shows more than 1.0. The sphericities
465 of all simulation results obtained from the drug and no-drug conditions in Figure 8A and
466 S17 were measured, and we found that the sphericities were decreased under EDTA and
467 blebbistatin (Fig. 8B, left panel). Similarly, the aspect ratios were increased under
468 EDTA and blebbistatin (Fig. 8C, left panel).

469 We searched for control parameters which can describe the sphericities or
470 aspect ratios. Among several parameters tested (Fig S19), the distances at potential
471 minima measured in Figure 7C showed a tight relationship to the sphericities (Fig. 8B,
472 right panel). The sphericities showed an abrupt change along the x-axis. These results
473 indicate that the sphericity is the order parameter for the morphological transition of the
474 compaction process and that the distance at the potential minimum is the control
475 parameter. On the other hand, the relative distances at 10% potential minima showed a
476 clear relationship to the aspect ratios (Fig. 8C, right panel). Thus, the morphological
477 transitions of the compaction process are induced by the quantitative changes in the DP

curves.

Modeling of distance–force curves

To comprehensively understand the effect of the differences of the DF curves on morphogenesis, we modeled the DF curves as a simple mathematical equation. We selected the following equation as described in SI (Section 6):

$$F(D) = \varepsilon(D - D_0)^{-N} \cos\left\{\frac{2\pi(D - D_0)}{\delta}\right\}, \text{ for } D > D_0 \qquad \text{(Eq. 4)}$$

Here, F is the force, D is the distance, and N is the exponent of D, affecting the decay of the DF curves along D (X-axis). D_0 and δ affect the profile of the DF curves as shown in Figure 9A. Specifically, D_0 can transform the DF curves along D, and δ affects the wavelength of the cosine function by which DEB is also introduced. All parameters and variables related to lengths/distances were normalized by (δ/4), leading to generation of dimensionless parameters and variables such as $D_0^* = D_0 /(\delta/4)$. This enabled us to present simulation outcomes in two-dimensional space (D_0^* and N) in a manner similar to a phase diagram (Fig. 9).

Systematic analyses of morphologies generated by distance–force curves

Using the DF curves defined by Equation 4, we systematically investigated

496 what kind of morphologies could be generated or stably maintained, and what kind of
497 morphological transformation could be achieved. Here, we tried to identify possible
498 stable states, including metastable states. We set various initial configurations of
499 particles, performed simulations under various DF curves, and then searched for local
500 minimum states. A cavity-bearing structure was set as the initial configuration (Fig. 9B
501 and S21-I). The simulation outcomes included cavity-bearing structures ("cavity" and
502 "cavity with extra particles"), cups, tubes, and lattices / aggregates as possible stable
503 states. Multiple clusters of particles were formed or disorganized morphologies were
504 generated which include distorted rings, etc. Importantly, when the DEBs were
505 eliminated from the DF curves, one of the cavity-bearing structures ("cavity"), cups, or
506 tubes were not generated (Fig. 9C), indicating that the DEBs are essential for the
507 formation or maintenance of these structures.

508 Next, we tried other initial configurations of particles. A two-dimensional sheet
509 was applied as the initial configuration which corresponds to a monolayered cell sheet
510 (Fig. 10). The simulation outcomes included spherically aggregated structures,
511 cavity-bearing structures, and two-dimensional sheets (Fig. 10A). In contrast to Figure
512 9B, the cavity-bearing structures were newly generated even in the absence of the DEBs
513 (Fig. 10B). DF curves were found, which can maintain the two-dimensional sheet, and

514 the maintenance was largely dependent on the DEBs (Fig. 10A vs. 10B). We confirmed
515 that the generated two-dimensional sheets were not broken by slight positional
516 fluctuations (Movie S7), indicating that the structures were stable.

517 Other analyses considering different initial configurations and/or different
518 particle numbers are shown in Figure S21. We also found that modulation of the profiles
519 of the DF curves can induce transition among some 2D and 3D structures such as 2D
520 sheet, bending sheet, aggregate etc. (Fig. S22, Movie S6, and SI, section 7-3).

521

522

523 Discussion

524 In this study, we developed a top-down method for statistically inferring
525 effective forces of cell–cell interactions using nuclear tracking data obtained from
526 microscopic images, which is applicable for non-equilibrium systems. We then
527 demonstrated that effective potentials of cell–cell interactions can be extracted from the
528 inferred forces in various living systems. Our findings provide for the first time the
529 experimental quantification of effective potentials, which have been recognized
530 conceptually (7, 10). Furthermore, we identified distances at potential minima as a
531 control parameter for describing the morphological transition during the compaction

process of mouse embryos, where sphericity was defined as an order parameter. By considering the qualitative and quantitative differences in the effective potentials, we successfully reproduced various three-dimensional structures, including cell aggregates, cavity-bearing structures, cups, tubes, two-dimensional sheets, etc. These structures are often observed during embryogenesis, morphogenesis, and organoids prior to the formation of complex tissue structures. For instance, cell aggregates are observed in early embryos in various species and spheroids (47–50); cavity-bearing structures in early embryos of various species, organoids, and cystic diseases (43, 47, 51–53); cell sheets in epithelia and germ layers (49, 54–56); tubes in tubular organs (57, 58); and cups in retina (i.e. optic cup) and murine epiblast (48, 59). Thus, we consider these structure as basic structural units for morphogenesis. These results suggest that the qualitative and quantitative differences in the effective potentials are powerful to explain the emergent properties of multicellular systems.

Effect of external factors on effective potentials

We detected DEBs in the effective potentials obtained from blastocysts and MDCK cysts, which are derived from indirect effect of cellular processes generating cavities on cell–cell interactions. In the case of the blastocysts, the trophectoderm cells

550 transport liquid from the outside of the embryos to the cavities, resulting in increased
551 hydrostatic pressure, and subsequent expansion of the cavities (35–37). Therefore, the
552 TE cells push each other through the liquid in the cavities. This indirect mechanical
553 repulsion might be reflected in the DEBs (Fig. S20 and S23A). In the case of the
554 MDCK cysts, tubes, and sheets, the DEBs may reflect properties of cell sheets as
555 discussed in Figure S23B.

556 How should we evaluate these indirect effects? Because cavities are generated
557 by cellular activities through liquid secretion, DEB is derived from cell intrinsic features.
558 However, the appearance of the DEBs depends on the existence of such external factors,
559 meaning that the DEBs are not derived from "real" interactions and thus their effects are
560 context-dependent. Our simulations using the potentials with the DEBs successfully
561 generated cavities, implying that some external factors can be approximately
562 incorporated into effective potentials. Nevertheless, the predictive capabilities of such
563 potentials should be carefully assessed. Our goal is to develop a framework for
564 explaining diverse morphogenesis in a minimal model. If indirect cell–cell interactions
565 provided from external factors could be approximately incorporated into effective
566 potential, the model based on effective potential might effectively reduce degrees of
567 freedom.

Comparison of other inference methods

To understand morphogenetic events, mechanical states and simulations based on those states are essential. Models such as vertex and Cellular Potts models are often utilized, especially for epithelial cells (3, 51, 60). These models successfully recapitulated various morphogenetic events, including the formation of the mouse blastocyst (60) and very early embryogenesis in *C.elegans* (61). However, it is still challenging to measure cellular and non-cellular parameters in three-dimensional systems with high spatiotemporal resolution, although high-resolution inferences of parameters such as cell–cell junction tensions and stresses have been performed in two-dimensional situations (33, 62). Our method enables to identify a control parameter from the effective potentials, and provides a framework for quantitatively connecting model parameters to *in vivo* parameters under three-dimensional situations.

Conclusion

Our framework, composed of the inference method and the particle-based model, has various potential uses for investigating the properties of cell–cell interaction,

586 material properties (Fig. 7C and S15), 3D morphogenesis (Fig. 6), 3D mechanical maps
587 (e.g. Fig. 3A), single-cell analysis of mechanics (e.g. Fig. 3A), relationships between
588 mechanical parameters and gene products (Fig. 7 and S5), and quantitative comparisons
589 of mechanical properties and behaviors among different living species and non-living
590 systems (Table S1, Fig. 6, and S12). Although some of these issues will be further
591 examined, we propose that our framework provides a novel physical scenario for
592 understanding the biophysics and physical biology of diverse morphogenetic events.
593
594
595 Acknowledgement
596 We thank Drs. Hitoshi Niwa and Yayoi Toyooka for providing the piggy-bac plasmids
597 and technical suggestions. We thank Drs. Jean-François Joanny, Hiroaki Takagi and
598 Yasuhiro Inoue for critical reading of the manuscript. We thank Dr. Yoshitaka Kimori
599 for helpful discussions. We thank Ms. Azusa Kato for supporting nuclear tracking. This
600 work was supported by following grants: Japan Ministry of Education, Culture, Sports,
601 Science and Technology Grant-in-Aid for Scientific Research on Innovative Areas
602 "Cross-talk between moving cells and microenvironment as a basis of emerging order"
603 for H.K., the National Institutes of Natural Sciences (NINS) program for

cross-disciplinary science study for H.K., a Japan Society for the Promotion of Science (JSPS) Grant-in-Aid for Young Scientists (B) for H.K. (17K15131), for Scientific Research (C) for T.O. (18K06234), and for Young Scientists (B) for T.O. (16K18544), a MEXT/JSPS Grant-in-Aid for Scientific Research on Innovative Areas for T.O. (17H05627), the Inamori Foundation for T.O., and the Takeda Science Foundation for T.O.

References

1. M. S. Steinberg, Differential adhesion in morphogenesis : a modern view. *Curr. Opin. Genet. Dev.* **17**, 1281–286 (2007).
2. C. Guillot, T. Lecuit, Mechanics of epithelial tissue homeostasis and morphogenesis. *Science (80-.).* **340**, 1185–9 (2013).
3. A. G. Fletcher, M. Osterfield, R. E. Baker, S. Y. Shvartsman, Vertex models of epithelial morphogenesis. *Biophys. J.* **106**, 2291–2304 (2014).
4. J.-L. Maître, *et al.*, Adhesion Functions in Cell Sorting by Mechanically Coupling the Cortices of Adhering Cells. *Science (80-.).* **338**, 253–256 (2012).
5. E. Bazellières, *et al.*, Control of cell–cell forces and collective cell dynamics by the intercellular adhesome. *Nat. Cell Biol.* **17**, 409–420 (2015).

6. J. Yong, *et al.*, Spatial distribution of cell–cell and cell–ECM adhesions regulates force balance while maintaining E-cadherin molecular tension in cell pairs. *Mol. Biol. Cell* **26**, 2456–2465 (2015).

7. G. Forgacs, S. A. Newman, *Biological Physics of the Developing Embryo* (Cambridge University Press, 2005).

8. X. Ma, *et al.*, Fibers in the extracellular matrix enable long-range stress transmission between cells. *Biophys. J.* **104**, 1410–1418 (2013).

9. X. Li, *et al.*, On the mechanism of long-range orientational order of fibroblasts. *Proc. Natl. Acad. Sci.* **114**, 8974–8979 (2017).

10. M. Merkel, M. L. Manning, Using cell deformation and motion to predict forces and collective behavior in morphogenesis. *Semin. Cell Dev. Biol.* **67**, 161–169 (2017).

11. T. R. Weikl, M. Asfaw, H. Krobath, R. Bartosz, R. Lipowsky, Adhesion of membranes via receptor–ligand complexes: Domain formation, binding cooperativity, and active processes. *Soft Matter* **5**, 3213–3224 (2009).

12. D. Drasdo, R. Kree, J. S. McCaskill, Monte Carlo approach to tissue-cell populations. *Phys. Rev. E* **52**, 6635–6657 (1995).

13. J. Ranft, *et al.*, Fluidization of tissues by cell division and apoptosis. *Proc. Natl.*

Acad. Sci. U. S. A. **107**, 20863–20868 (2010).

14. N. Sepúlveda, *et al.*, Collective Cell Motion in an Epithelial Sheet Can Be Quantitatively Described by a Stochastic Interacting Particle Model. *PLoS Comput. Biol.* **9**, e1002944 (2013).

15. B. Szabó, *et al.*, Phase transition in the collective migration of tissue cells: Experiment and model. *Phys. Rev. E* **74**, 061908 (2006).

16. J. M. Belmonte, G. L. Thomas, L. G. Brunnet, R. M. C. de Almeida, H. Chate, Self-Propelled Particle Model for Cell-Sorting Phenomena. *Phys. Rev. Lett.* **100**, 248702 (2008).

17. S. B. Nissen, S. Rønhild, A. Trusina, K. Sneppen, Theoretical tool bridging cell polarities with development of robust morphologies. *Elife* **7**, e38407 (2018).

18. J. Delile, M. Herrmann, N. Peyriéras, R. Doursat, A cell-based computational model of early embryogenesis coupling mechanical behaviour and gene regulation. *Nat. Commun.* **8**, 13929 (2017).

19. J. Kashef, C. M. Franz, Quantitative methods for analyzing cell–cell adhesion in development. *Dev. Biol.* **401**, 165–174 (2015).

20. S. Garcia, *et al.*, Physics of active jamming during collective cellular motion in a monolayer. *Proc. Natl. Acad. Sci. U. S. A.* **112**, 15314–15319 (2015).

21. M. Basan, J. Elgeti, E. Hannezo, W.-J. Rappel, H. Levine, Alignment of cellular motility forces with tissue flow as a mechanism for efficient wound healing. *Proc. Natl. Acad. Sci.* **110**, 2452–2459 (2013).

22. E. Schötz, *et al.*, Quantitative differences in tissue surface tension influence zebrafish germ layer positioning. *HFSP J.* **2**, 42–56 (2008).

23. B. He, K. Doubrovinski, O. Polyakov, E. Wieschaus, Apical constriction drives tissue-scale hydrodynamic flow to mediate cell elongation. *Nature* **508**, 392–396 (2014).

24. Y. Arboleda-Estudillo, *et al.*, Movement Directionality in Collective Migration of Germ Layer Progenitors. *Curr. Biol.* **20**, 161–169 (2010).

25. M. Basan, J. Prost, J.-F. Joanny, J. Elgeti, Dissipative particle dynamics simulations for biological tissues: rheology and competition. *Phys. Biol.* **8**, 026014 (2011).

26. Z. Bao, *et al.*, Automated cell lineage tracing in Caenorhabditis elegans. *Proc. Natl. Acad. Sci. U. S. A.* **103**, 2707–2712 (2006).

27. K. McDole, *et al.*, In Toto Imaging and Reconstruction of Post-Implantation Mouse Development at the Single-Cell Level. *Cell* **175**, 859-876.e33 (2018).

28. F. Amat, P. J. Keller, Towards comprehensive cell lineage reconstructions in

complex organisms using light-sheet microscopy. *Dev. Growth Differ.* **55**, 563–578 (2013).

29. K. Kyoda, *et al.*, WDDD: Worm developmental dynamics database. *Nucleic Acids Res.* **41**, D732-7 (2013).

30. Y. Kurotaki, K. Hatta, K. Nakao, Y.-I. Nabeshima, T. Fujimori, Blastocyst axis is specified independently of early cell lineage but aligns with the ZP shape. *Science* **316**, 719–23 (2007).

31. B. M. Pettitt, P. J. Rossky, Alkali halides in water: Ion–solvent correlations and ion–ion potentials of mean force at infinite dilution. *J. Chem. Phys.* **84**, 5836–5844 (1986).

32. J. N. Israelachvili, *Intermolecular and Surface Forces*, 3rd ed. (Elsevier Inc., 2011).

33. S. Ishihara, K. Sugimura, Bayesian inference of force dynamics during morphogenesis. *J. Theor. Biol.* **313**, 201–211 (2012).

34. S. J. Fletcher, *Data Assimilation for the Geosciences: From Theory to Application*, 1st ed. (Elsevier, 2017).

35. K. Moriwaki, S. Tsukita, M. Furuse, Tight junctions containing claudin 4 and 6 are essential for blastocyst formation in preimplantation mouse embryos. *Dev*

Biol **312**, 509–22 (2007).

36. X. Wang, *et al.*, Characterizing Inner Pressure and Stiffness of Trophoblast and Inner Cell Mass of Blastocysts. *Biophys. J.* **115**, 2443–2450 (2018).

37. J. G. Dumortier, *et al.*, Hydraulic fracturing and active coarsening position the lumen of the mouse blastocyst. *Science (80-.).* **365**, 465–468 (2019).

38. Y. Arata, H. Takagi, Y. Sako, H. Sawa, Power law relationship between cell cycle duration and cell volume in the early embryonic development of Caenorhabditis elegans. *Front. Physiol.* **5**, 529 (2015).

39. L. G. Edgar, Blastomere Culture and Analysis. *Methods Cell Biol.* **48**, 303–321 (1995).

40. E. Schierenberg, B. Junkersdorf, The role of eggshell and underlying vitelline membrane for normal pattern formation in the early C. elegans embryo. *Roux's Arch. Dev. Biol.* **202**, 10–16 (1992).

41. J. C. Fierro-González, M. D. White, J. C. Silva, N. Plachta, Cadherin-dependent filopodia control preimplantation embryo compaction. *Nat. Cell Biol.* **15**, 1424–33 (2013).

42. R. Kawagishi, *et al.*, Na+/H+ exchanger-3 is involved in mouse blastocyst formation. *J. Exp. Zool. Part A Comp. Exp. Biol.* **301**, 767–775 (2004).

43. A. Z. Wang, G. K. Ojakian, W. J. Nelson, Steps in the morphogenesis of a polarized epithelium. *J. Cell Sci.* **95**, 137–152 (1990).

44. J. Kim, *et al.*, Evaluation of morphokinetic characteristics of zona pellucida free mouse pre-implantation embryos using time-lapse monitoring system. *Int. J. Dev. Biol.* **64**, 415–422 (2020).

45. J.-L. Maître, R. Niwayama, H. Turlier, F. Nédélec, T. Hiiragi, Pulsatile cell-autonomous contractility drives compaction in the mouse embryo. *Nat. Cell Biol.* **17**, 849–855 (2015).

46. M. Takeichi, The cadherins : cell-cell adhesion molecules controlling animal morphogenesis. **655** (1988).

47. H. Honda, T. Nagai, M. Tanemura, Two different mechanisms of planar cell intercalation leading to tissue elongation. *Dev. Dyn.* **237**, 1826–1836 (2008).

48. M. Eiraku, *et al.*, Self-organizing optic-cup morphogenesis in three-dimensional culture. *Nature* **472**, 51–6 (2011).

49. C. Pérez-González, *et al.*, Active wetting of epithelial tissues. *Nat. Phys.* **15**, 79–88 (2019).

50. F. Montel, *et al.*, Stress Clamp Experiments on Multicellular Tumor Spheroids. *Phys. Rev. Lett.* **107**, 188102 (2011).

51. J. M. Belmonte, *et al.*, Virtual-tissue computer simulations define the roles of cell adhesion and proliferation in the onset of kidney cystic disease. *Mol. Biol. Cell* **27**, 3673–3685 (2016).

52. N. C. Rivron, *et al.*, Blastocyst-like structures generated solely from stem cells. *Nature* **557**, 106–111 (2018).

53. D. Serra, *et al.*, Self-organization and symmetry breaking in intestinal organoid development. *Nature* **569**, 66–72 (2019).

54. D. Drasdo, S. Höhme, A single-cell-based model of tumor growth in vitro: monolayers and spheroids. *Phys. Biol.* **2**, 133–147 (2005).

55. P. Vitorino, M. Hammer, J. Kim, T. Meyer, A Steering Model of Endothelial Sheet Migration Recapitulates Monolayer Integrity and Directed Collective Migration. *Mol. Cell. Biol.* **31**, 342–350 (2011).

56. M. Smutny, *et al.*, Friction forces position the neural anlage. *Nat. Cell Biol.* **19**, 306–317 (2017).

57. R. Montesano, G. Schaller, L. Orci, Induction of epithelial tubular morphogenesis in vitro by fibroblast-derived soluble factors. *Cell* **66**, 697–711 (1991).

58. H. Koyama, *et al.*, Mechanical Regulation of Three-Dimensional Epithelial Fold

Pattern Formation in the Mouse Oviduct. *Biophys. J.* **111**, 650–665 (2016).

59. L. Solnica-krezel, D. S. Sepich, Gastrulation: Making and Shaping Germ Layers. *Annu. Rev. Cell Dev. Biol.* **28**, 687–717 (2012).

60. H. Honda, N. Motosugi, T. Nagai, M. Tanemura, T. Hiiragi, Computer simulation of emerging asymmetry in the mouse blastocyst. *Development* **135**, 1407–1414 (2008).

61. A. Kajita, M. Yamamura, Y. Kohara, Computer simulation of the cellular arrangement using physical model in early cleavage of the nematode Caenorhabditis elegans. *Bioinformatics* **19**, 704–716 (2003).

62. D. T. Tambe, *et al.*, Collective cell guidance by cooperative intercellular forces. *Nat. Mater.* **10**, 469–75 (2011).

Figures

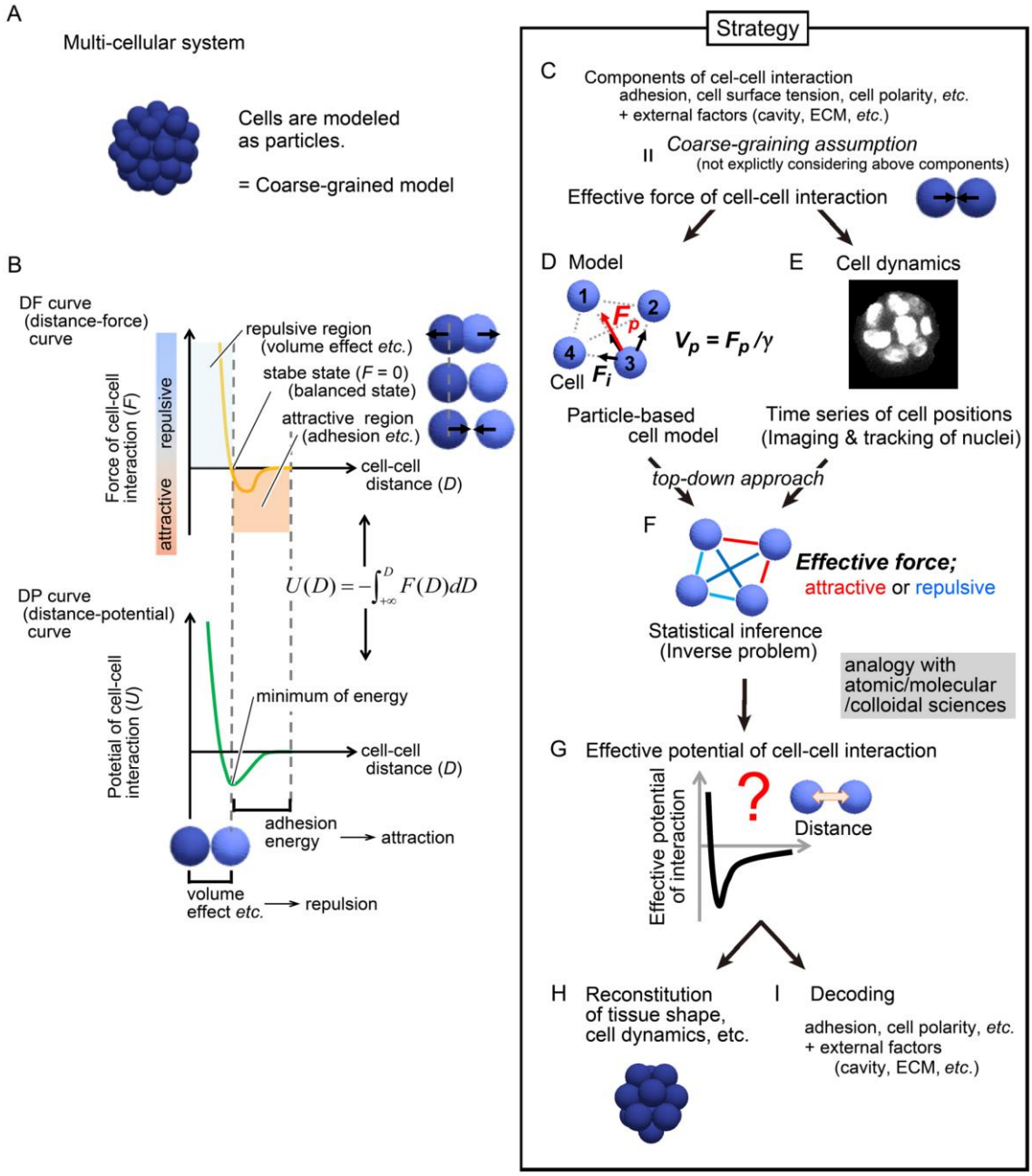

Figure 1: Overview of strategy for inferring the effective potential of cell–cell interactions

A. Cells were modeled as particles. A blue sphere corresponds to a cell. B. Distance–

768 force (DF) and distance–potential (DP) curves are considered. Typical profiles of the
769 curves, their physical meaning, and their origins are shown. C-I. Strategy for inferring
770 effective forces of cell–cell interactions is described. C. Mechanics of cell–cell
771 interactions is coarse-grained, leading to effective forces of cell–cell interactions as
772 shown in D. Detailed conceptual explanations are described in Figure S1. D. attractive
773 or repulsive force between the particles (blue spheres #1–4), was considered; force
774 vectors (F_i) are illustrated by black arrows in the case of particle #3. The net force (F_p)
775 is shown by a red vector, and the relationship between F_p and velocity (V_p) is described.
776 E. From a time series of microscopic images of nuclei, nuclear tracking data were
777 obtained. F. Effective forces of cell–cell interactions were inferred by solving an inverse
778 problem. The inference method is explained in Figure S2. G. The inferred force values
779 (F) were plotted against the distance between cell–cell interactions, and whether DF or
780 DP curves are emerged from the plots were examined. H. Whether the DF or DP curves
781 can reconstitute tissue shape or cell dynamics was examined. Components related to
782 cell–cell interactions described in C can be decoded from the DF or DP curves was
783 tested.
784 Related figure: Figure S1 and S2.
785

786

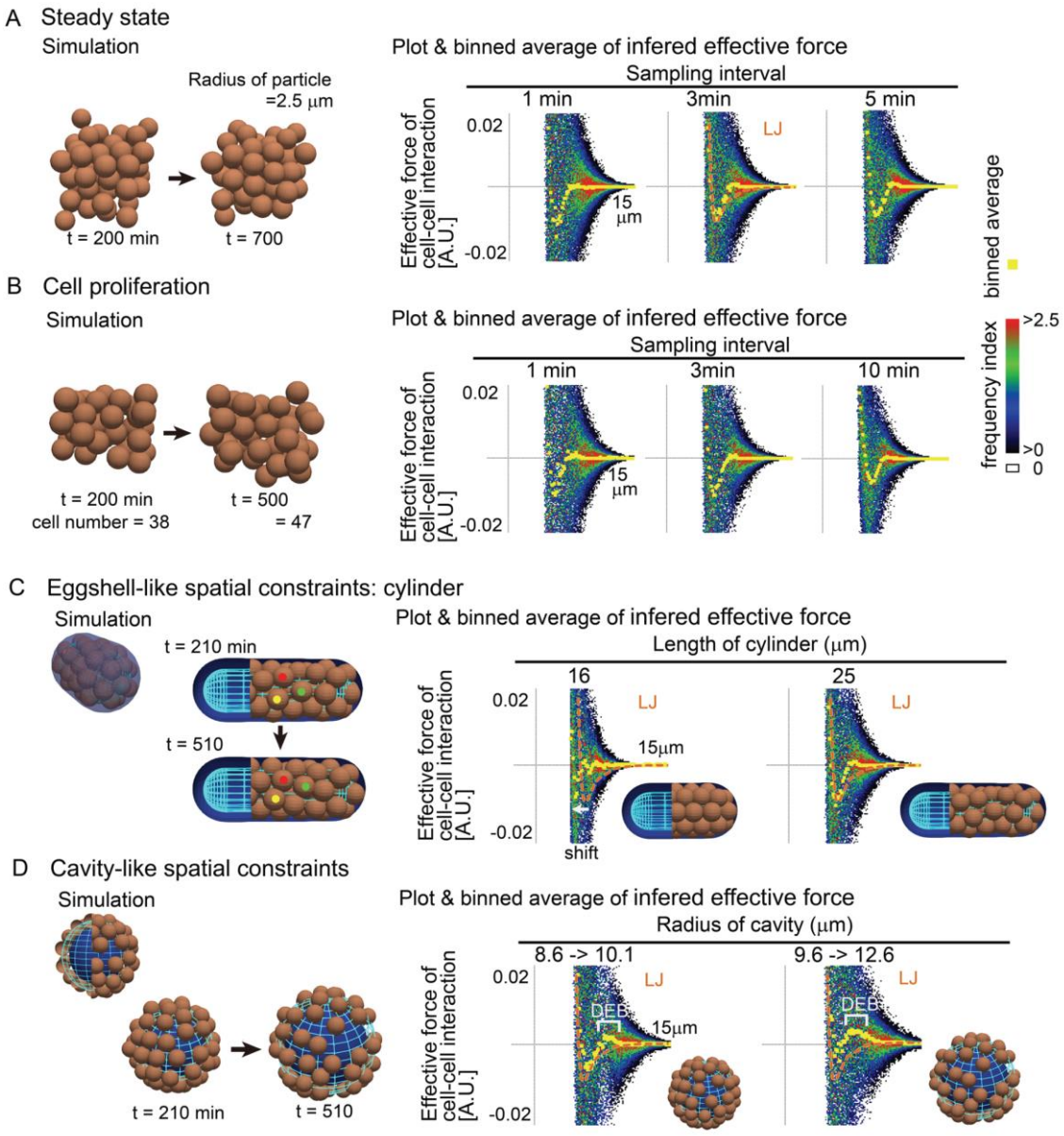

Figure 2: Validation of inference method using simulation data

Simulations were performed on the basis of a distance–force (DF) curve obtained from the Lenard-Jones potential (LJ). The simulation conditions contain “Steady state” (A),

793 “Cell proliferation” (B), “Egg shell-like spatial constraints” (C), and “Cavity-like spatial
794 constraints” (D). The left panels in A-D are snapshots of the simulations. The right
795 panels in A-D are DF curves obtained from the inference. Effective forces of
796 interactions for each pair of cells for each time frame were plotted against the distance
797 of the cell–cell interactions, and shown as a colored heat map representing the
798 frequencies of the data points (Frequency index (FI)). Averaged values of the forces are
799 shown in yellow (binned average). Detailed procedures are described in SI (Section 5).
800 In some graphs, the DF curves from the LJ potential are overlaid by orange broken lines
801 (LJ). In A and B, simulation data with different sampling intervals were applied. In C,
802 under the cylindrical constraint with a shorter length where particles are highly
803 compressed, the DF curve was shifted leftward along the distance (white arrow). In D,
804 on the expanding cavities, repulsive forces at distant regions were detected, which we
805 called distant energy barriers (DEB). Related comprehensive analyses are shown in
806 Figure S4 which also demonstrated that the DEBs are derived from the cavities.
807 Detailed assumptions and conditions of the simulations are described in SI, Section 7-4.
808 Related figures: Figure S3, S4, and S5. Related movies: Movie S1A-C, S2A-B, and
809 S8A-D.
810

811

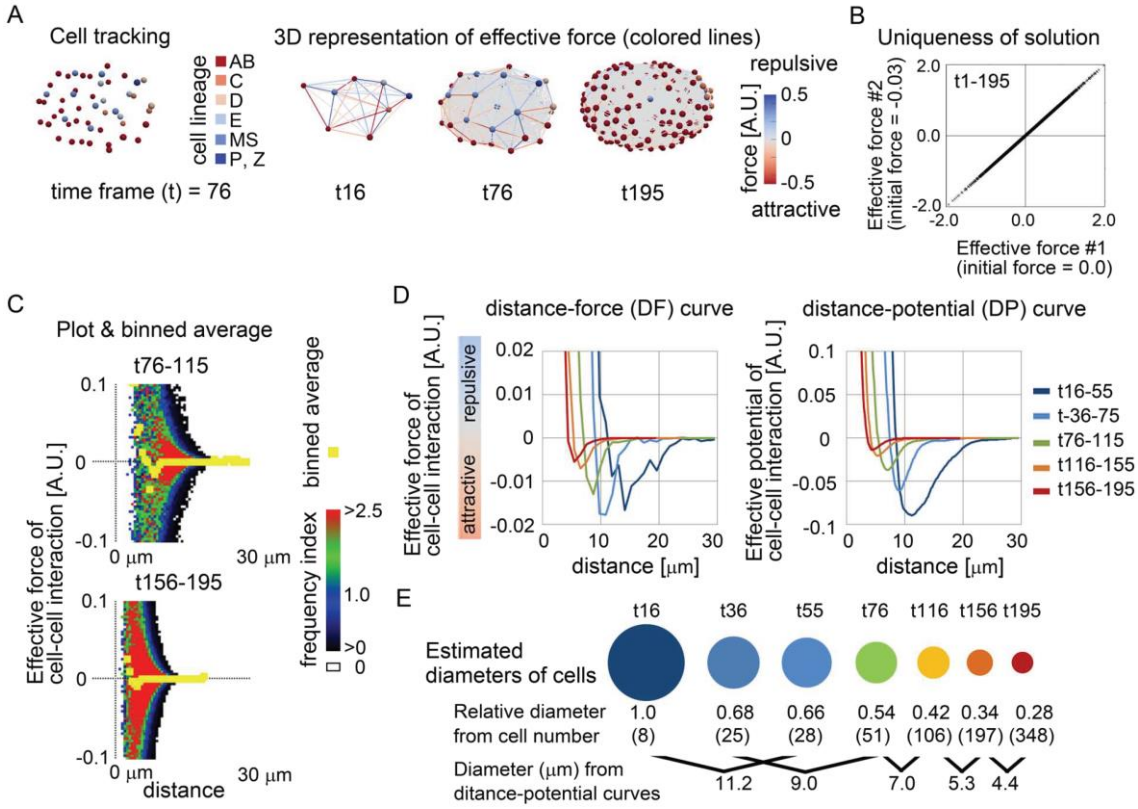

Figure 3: Inference of effective force of cell–cell interaction in *C.elegans* embryos

A. Snapshot of the nuclear positions in the *C.elegans* embryo (left panel) and snapshots with inferred effective forces (right three panels) were three-dimensionally visualized at the time frames as described (t16, t76, and t195); the interval between time frames is 1 min. The spheres correspond to cells whose colors represent cell lineages, including AB, C, D, E, MS, and P & Z. The lines represent cell–cell interactions; the colors indicate the values of the effective forces (red, attractive; blue, repulsive). Forces are depicted in arbitrary units (A.U.); 1 A.U. of the force can move a particle at 1μm/min as described

823 in SI (Section 4-4). The nuclear tracking data were obtained from a previous report (26).
824 Related figures and movies are provided (Fig. S6A, B, Movies S3A and B). B.
825 Uniqueness of solution of effective force inference was examined. The minimizations of
826 Equation S6 were performed from different initial force values as described in the x-
827 and y- axes, and the inferred values of each cell-cell interaction were plotted by crosses.
828 C. The inferred effective forces of cell–cell interactions were plotted against the
829 distance of cell–cell interactions in a manner similar to Figure 2. The graphs for time
830 frame 76–115 and 156–195 are shown. Data at other time frames are provided in Figure
831 S6C. D. Distance–force (DF) and distance–potential (DP) curves were estimated.
832 Details are described in SI (Section 5-3). The curves for each time frame are shown. E.
833 Mean diameters of cells at each time frame were estimated from cell numbers and the
834 DP curves. Given that the volume of the embryos is constant (= *Vol*) during
835 embryogenesis, the mean diameters were estimated from the cell numbers (N_c) at each
836 time frame as follows: mean diameter = $\{Vol / (4/3\ \pi\ N_c)\}^{1/3}$. The diameters relative to
837 that at time frame = 16 are shown with cell numbers (parentheses). The sizes of the
838 circles reflect the diameters, whose colors roughly correspond to the colors in the graph
839 in D. The diameters were also estimated from the DP curves in D; the distances at
840 minima of the DP curves roughly reflect the diameters (Fig. 1B and S2D).

Related figure: Figure S6. Related movies: Movie S3A-B.

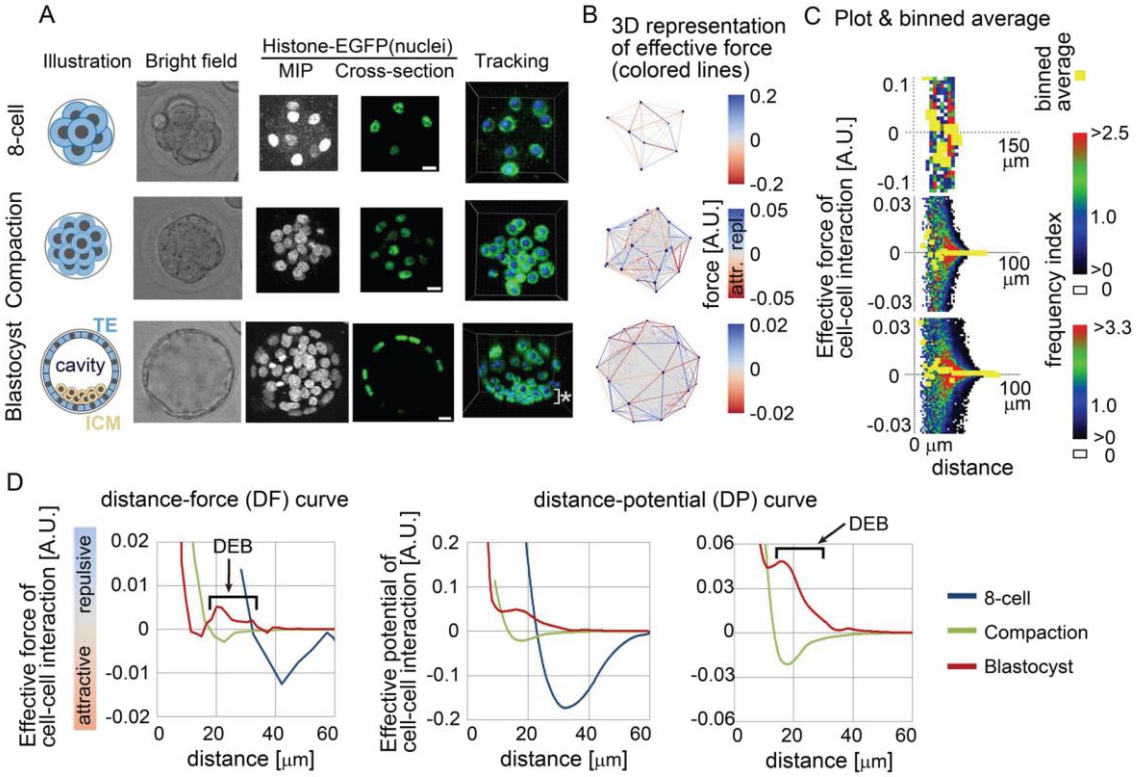

Figure 4: Inference of the effective force of cell–cell interaction in mouse pre-implantation embryos

A. Eight-cell, compaction, and blastocyst stages of mouse embryo are illustrated, and their confocal microscopic images are shown: bright field, maximum intensity projection (MIP) and cross-section of fluorescence of H2B-EGFP. Snapshots of nuclear tracking are also shown; blue spheres indicate the detected nuclei. In the nuclear tracking image of the blastocyst, ICM cells are located around the bottom region of the image, as indicated by *. Scale bars = 15µm. Related movies are provided (Movie S4A–

855 C). B. Snapshots of nuclear positions with inferred effective forces were visualized
856 three-dimensionally for the three embryonic stages in a manner similar to Figure 3A.
857 Related movies are provided (Movie S4D-G). The uniqueness of the solutions was
858 confirmed in Figure S7B. C. The inferred effective forces of cell–cell interactions were
859 plotted against the distance of cell–cell interactions in a manner similar to Figure 2. D.
860 Distance–force (DF) and distance–potential (DP) curves were estimated from (C) in a
861 manner similar to Figure 3D. A distant energy barrier (DEB) was detected, as indicated
862 by arrows. Data from other embryos are provided in Figure S7A. The differences in DF
863 and DP curves between ICM and TE cells and between the outer and inner cells in the
864 compaction state were described in Figure S8. DP curves between adjacent cells are
865 provided in Figure S9. DP curves from the embryos whose cavitation was inhibited by
866 chemicals are shown in Figure S20.
867 Related figures: Figure S7, S8, S9, and S20. Related movies: Movie S4A-G.
868

869

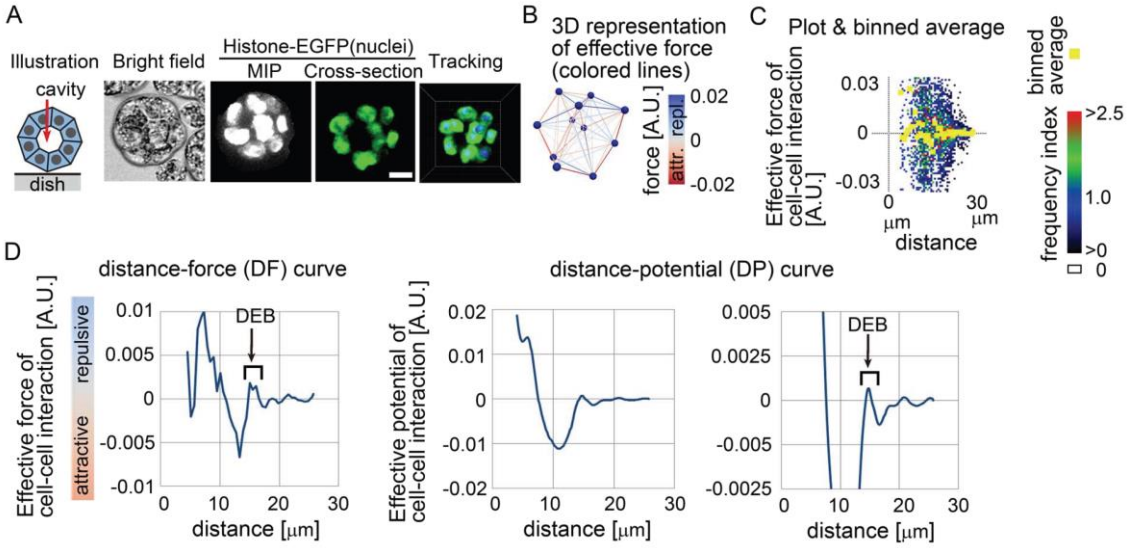

870

871

872 Figure 5: Inference of effective force of cell–cell interaction in cysts formed by MDCK

873 cells

874 A. MDCK cysts formed under suspension conditions are illustrated, and confocal

875 microscopic images are shown: bright field, maximum intensity projection (MIP) and

876 cross-section of fluorescence of H2B-EGFP. A snapshot of nuclear tracking is also

877 shown; blue spheres represent nuclei. Scale bars = 10μm. A related movie is provided

878 (Movie S5A). B. A snapshot of the nuclear positions with inferred effective forces was

879 three-dimensionally visualized in a manner similar to Figure 3A. The blue spheres

880 correspond to cells. The lines represent cell–cell interactions and the colors indicate the

881 values of the effective forces [red, attractive (attr.); blue, repulsive (repl.)]. A related

882 movie is provided (Movie S5B). The uniqueness of the solutions was confirmed in
883 Figure S10B. C. The inferred effective forces of cell–cell interaction were plotted
884 against the distance of cell–cell interaction in a manner similar to Figure 3C. D.
885 Distance–force and distance–potential curves were estimated from (C) in a manner
886 similar to Figure 3D. DEB was detected as indicated by arrows. Data from other cysts
887 are provided in Figure S10A. DP curves between adjacent cells are provided in Figure
888 S11.
889 Related figures: Figure S10 and S11. Related movies: Movie S5A-B.
890
891

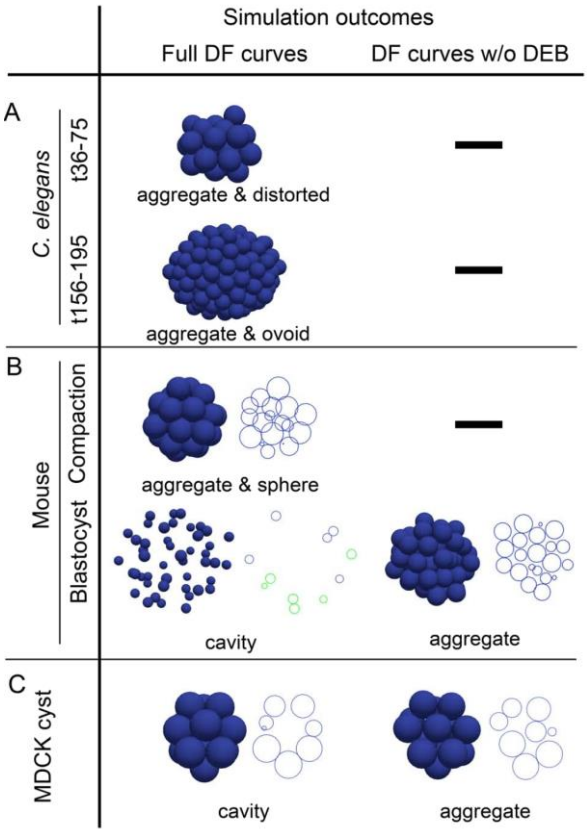

Figure 6: Outcomes of simulations based on inferred distance–force curves

Simulations results under the DF curves derived from *C. elegans* (A) and mouse embryos (B), and the MDCK cyst (C) are shown. Blue spheres correspond to cells. In the *C. elegans* embryos, the DF curves were derived from time frames 36–75 and 156–195 in Figure 3D. In the mouse embryos, the DF curves were derived from the compaction and blastocyst stages in Figure 4D. Cross-sections are also visualized. In the case of the mouse blastocyst, two parallel cross-sections (shown in blue and green)

902 are merged. In the MDCK cyst, the DF curves are derived from Figure 5D. In the
903 blastocyst and the MDCK cyst, the DF curves without DEB were also applied (w/o
904 DEB). The diameters of the blue spheres are set to be equivalent to the distance at the
905 minimum potential (Fig. S2D). The initial configurations of the simulations are
906 described in Figure S12, along with other simulation results.
907 Related figure: Figure S12.
908
909

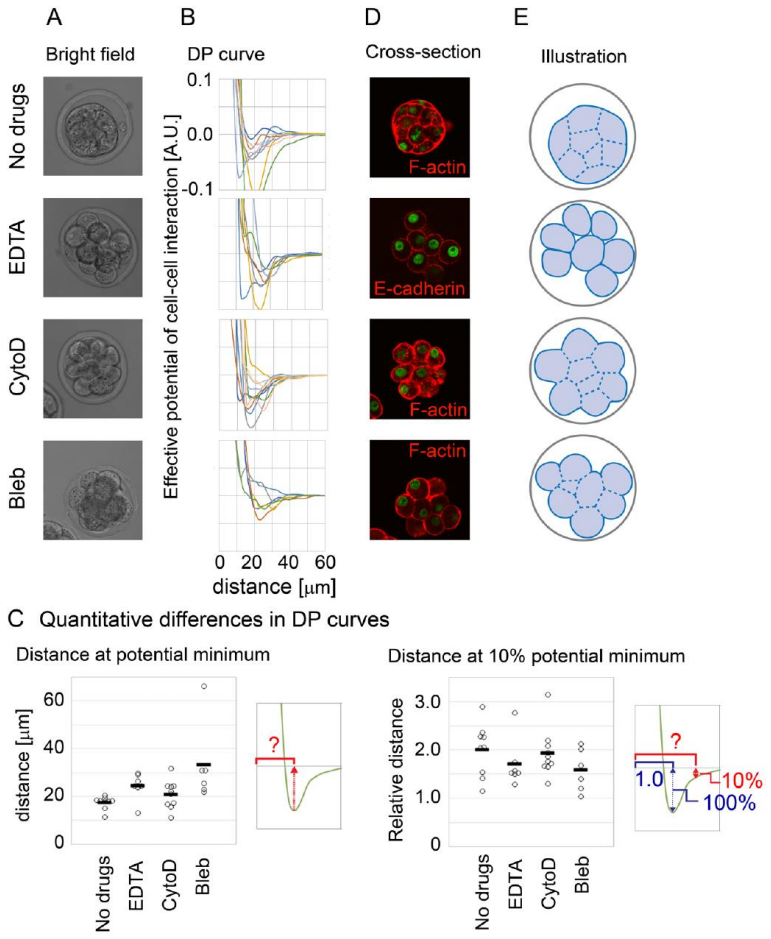

Figure 7: Inference of effective potentials of cell–cell interaction in compaction-inhibited mouse embryos

A. Microscopic images of embryos are shown, where the compaction states were inhibited by chemicals. The experimental design is described in Figure S13. CytoD, cytochalasin D; Bleb, blebbistatin. B. DP curves of the drug-treated embryos are shown. N=6~10 for each condition. Enlarged views are provided in Figure S14. C. Quantitative

differences in the DP curves were calculated. Distances at the potential minima in the DP curves are plotted (left panel). Distances providing 10% energy of the potential minima are plotted as the relative value to the distances at the potential minima (right panel). Mann–Whitney–Wilcoxon tests were performed (SI, Section 5-4-2) and the resultant *p*-values for “No Drugs” vs. “EDTA”, vs. “CytoD”, and vs. “Bleb” are 0.011, 0.23, and 0.00040, respectively, in the left panel. The *p*-values in the right panel are shown in Figure S15B. Other quantification data are provided in Figure S15, S24, and Table S1. D. Confocal microscopic images of cell shapes in the drug-treated embryos are shown. Cell shapes were visualized by staining F-actin or E-cadherin. Other images of staining are provided in Figure S16. E. The embryonic and cellular shapes in the drug-treated embryos are illustrated based on D.

Related figures: Figure S13, S14, S15, S16, S24, and Table S1.

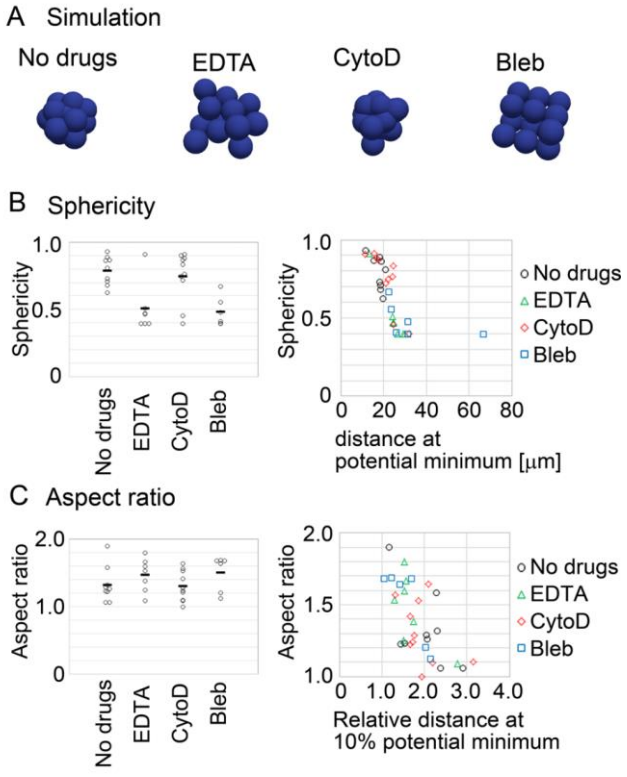

Figure 8: Simulations under inferred distance–potential curves in drug-treated embryos, and identification of parameters explaining morphological transition

A. Simulation results for the drug-treated embryos are shown. All simulation data are provided in Figure S17, and the representative results which nearly showed the mean values of the sphericities for each condition are chosen here. Simulation results from a different initial configuration was provided in Figure S17. B. Sphericities in the simulations of the drug-treated embryos were calculated (left panel), and the sphericities were plotted against the distances at the potential minima calculated in Figure 7C.

Mann–Whitney–Wilcoxon tests were performed (SI, Section 5-4-2) and the resultant *p*-values for “No Drugs” vs. “EDTA”, vs. “CytoD”, and vs. “Bleb” are 0.011, 1.0, and 0.00080, respectively, in the left panel. Relationships between the sphericities and other parameters are shown in Figure S19. C. Aspect ratios in simulations of the drug-treated embryos were calculated (left panel), and the aspect ratios were plotted against the relative distances providing 10% energy of the potential minima which were calculated in Figure 7C. Mann–Whitney–Wilcoxon tests were performed (SI, Section 5-4-2) and the resultant *p*-values for “No Drugs” vs. “EDTA”, vs. “CytoD”, and vs. “Bleb” are 0.21, 0.97, and 0.33, respectively, in the left panel. Relationships between the aspect ratios and other parameters are shown in Figure S19. Sphericities and aspect ratios from the different initial configuration of the simulation are provided in Figure S18.

Related figures: Figure S17, S18, and S19.

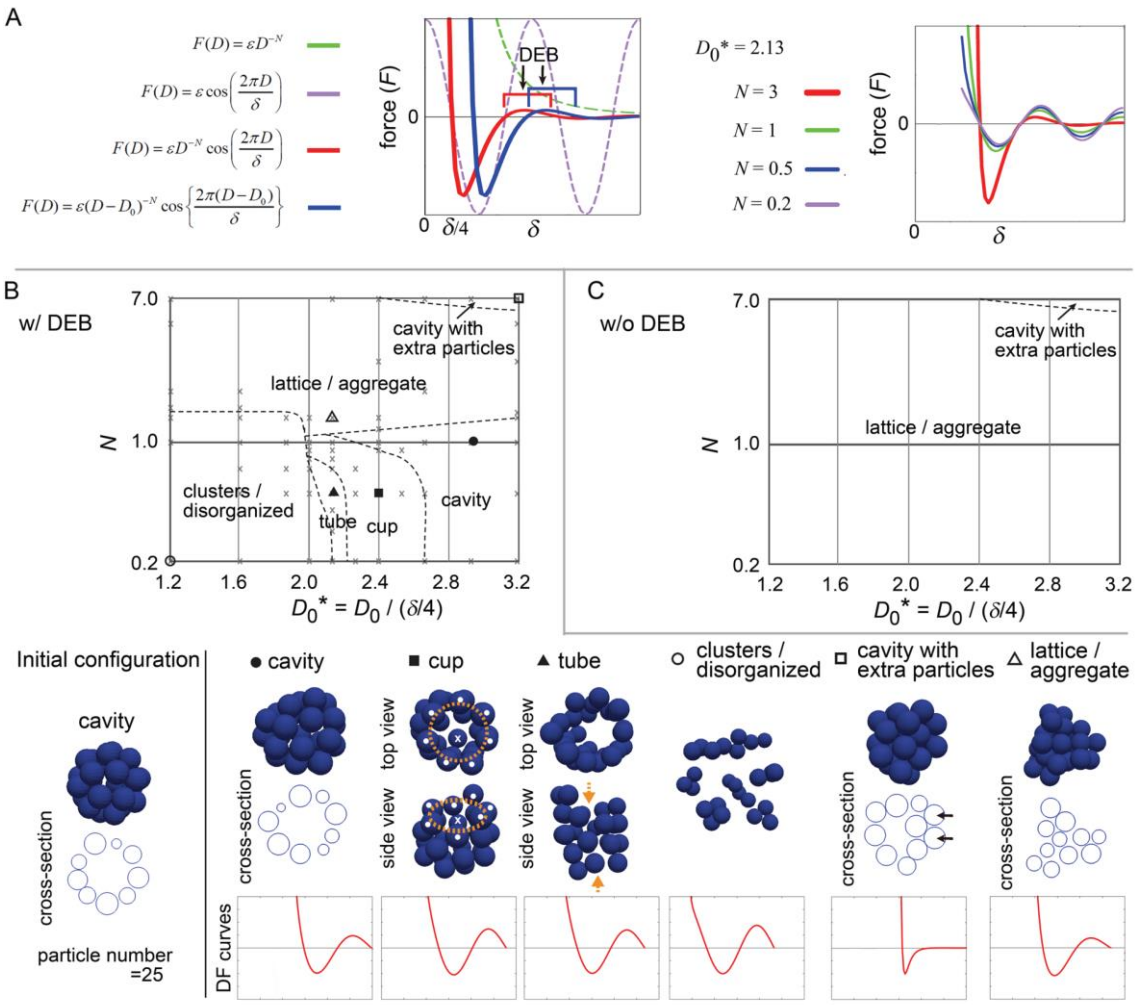

Figure 9: Modeling of distance–force curves and diagrams of simulation outcomes

A. DF curves were mathematically modeled using four parameters: N, D_0, δ, and ε. In the case of the DF curves without the cosine term, the curves ($F = \varepsilon\ (D - D_0)^{-N}$) are always >0 (repulsive) (green broken line). Upon introduction of the cosine (purple broken line), the curves acquire regions with <0 (attractive) and DEB (red line). Upon

introduction of D_0, the curves are translated along the distance (blue line). N affects the gradient of the curves and the height of DEB (right panel). DF curves from $D = 0$ to D at the end of DEB (w/ DEB) or the curves from $D = 0$ to D before starting DEB (w/o DEB) were used in the following simulations. B. Outcomes of simulations under various values of N and D^* are shown in the diagrams. A cavity-bearing structure was given as an initial configuration; the blue spheres correspond to cells, and a cross-section is visualized. According to the conditions, a cavity was maintained, whereas cups, tubes, etc. were generated. Some conditions on the diagram were designated by symbols (circle, square, and triangle), and their simulation results are visualized (blue spheres). Example profiles of the DF curves are shown. The diameters of the blue spheres are set to be 0.5× the distance at the minimum potential, which corresponds to the distance with $F = 0$ (arrows in the profiles of the DF curves, Fig. S2D). In the case of the cup, the mouth of the cup is marked by orange rings, and the particles located on the ring are labeled by white dots. Note that the particles labeled particles by crosses are located neither on the ring nor at the center of the ring. In the case of the tube, the open ends of the tube are shown by orange arrows. In the case of the cavity with extra particles, the extra particles are shown by arrows. The definition of each phase (i.e. the cavity, cup, etc.) is explained in SI (section 7-2). Data points for

depicting the lines separating each phase are shown by gray crosses. A phase diagram under different numbers of particles is provided in Figure S21-I-A, where the overall relative positions among the phases were conserved though the parameter values for generating each phase became different. C. Simulation outcomes are shown on diagrams similar to B, except that the simulations were performed without DEBs.

Related figure: Figure S21-I.

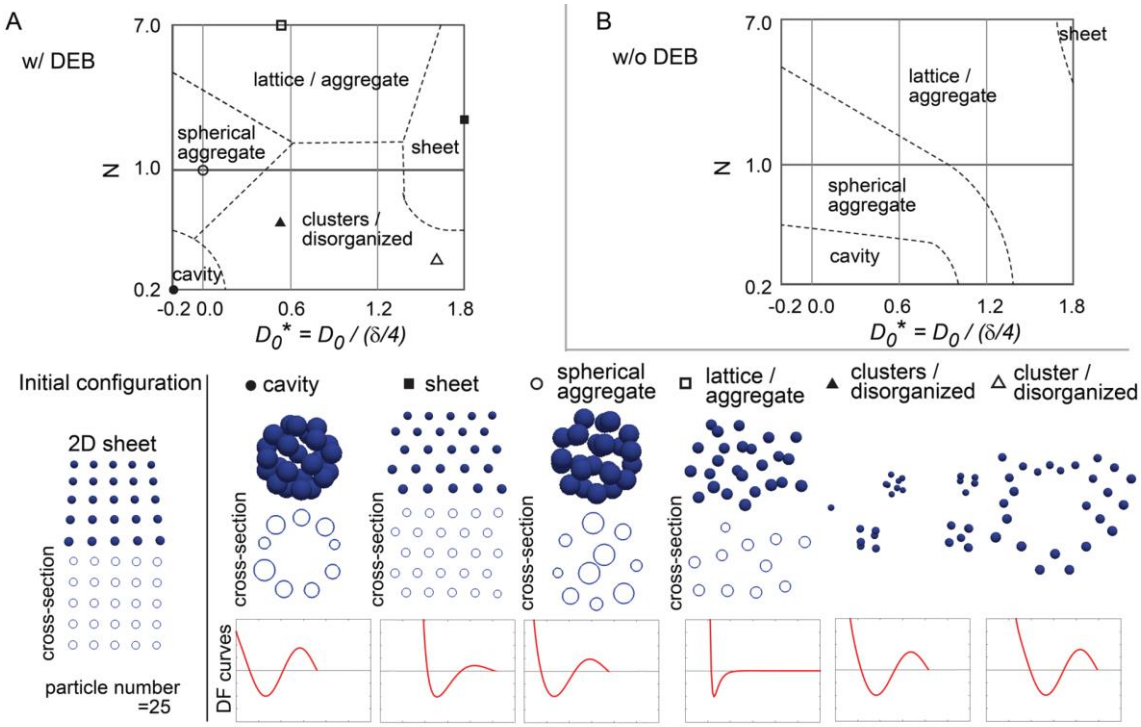

Figure 10: Simulation outcomes and their diagrams, based on distance–force curves; starting from 2D sheet

A. Simulations were performed from a two-dimensional (2D) sheet with slight positional fluctuations under various distance–force curves defined by Equation 4 (Fig. 9A), and a diagram of the outcomes is shown. The number of particles was set to 25. Cross-sections are also presented (blue circles). According to the conditions, the 2D sheet was maintained, whereas aggregates, cavity-bearing structures etc. were generated. The diameters of the blue spheres are set to be 0.2× the distance at the potential

minimum.

B. Similar to A, except that the simulations were performed without distant energy barriers (DEBs). 2D sheets were maintained, but the area in the diagram became significantly smaller than that in A. Other diagrams are provided in Figure S21. Possible shape transformations are exemplified in Figure S22.

Related figures: Figure S21-II, S22, and S23. Related movie: Movie S6.